ENHANCEMENTS TO THE INHERENT STRAIN METHOD FOR ADDITIVE MANUFACTURING ANALYSIS

*Qiukai Lu, Erwan Beauchesne, & Tadeusz Liszka**

Altair Engineering, Austin, TX, 78757

*Address all correspondence to: Tadeusz Liszka, Altair Engineering, 7800 Shoal Creek Blvd 200N, Austin, TX, 78757, E-mail: tad@altair.com

Analysis of stress and deformation of parts produced during additive manufacturing (AM) process is critical to predict potential defects during the process and quality of parts produced. However, the complex physics of the process and vastly different scales of the analysis require long computations on powerful computers (including exa-scale computing), which makes accurate analysis impractical. Simplified approach in published literature typically utilizes extrapolation of inherent strain theory developed for analysis of welding processes, however, results are often unsatisfactory as the AM process and geometry of produced parts is much more complex. Here we present generalization of the inherent strain into a two-level method, where the fine model (so-called mesoscale analysis) provides a whole family of inherent strain models, and the coarse model (macroscale) uses different values for inherent strain varying with location, surrounding geometry, and parameters of AM process.

KEY WORDS: *additive manufacturing, inherent strain method*

1. INTRODUCTION

This paper focuses on the analysis of powder bed-based additive manufacturing (AM) processes, such as selective laser melting (SLM) Shapiro et al. (2016), where a product (final part with the complex shape) is built layer by layer by local melting of the metal powder using high energy lasers. High accuracy modeling of such process can only be attempted using exa–scale computer models (John et al., 2017) for practical design and manufacturing solutions it is necessary to utilize significant simplifications in the process (Ferencz et al., 2017). Numerical modeling of AM processes, in the context of engineering analysis, is based on techniques developed over the last 50 years for the metal welding processes (Argyris et al., 1982; Friedman, 1975), and focuses on analysis of stresses caused by the deposition process (Lundbäck, 2010; Ueda et al., 2012; Yuan and Ueda, 1996).

Conceptually the piece is built by adding microscopic drops of melted metal and eventually filling the total volume of the desired model. Each drop of melted metal has the size of tens of micrometers, while the part size is in the order of hundreds of millimeters. As a result of this difference in scales, the global finite element model (macro–scale) in order to be solvable in acceptable time, has to use finite elements that represent several (10 or more) layers of powder. Thus, at the macroscale solution, the only meaningful choice is to activate simultaneously whole layers of elements. The actual behavior of metal at the finer scale(s) is approximated through the inherent strain method, which applies some initial strain during activation of each new element.

Use of multiscale processing for accurate evaluation of effective properties of heterogeneous media with microstructure has been extensively studied, allowing estimation of the limits of effective properties depending on proper choice of representative volume (RV) dimensions and boundary conditions (Hill, 1963) and further refined to account for statistical properties of the microstructure (Kale et al., 2015). Under these assumptions, the solution at the fine scale is performed very accurately, using one set of material properties and process parameters (Hodge and

Ferencz, 2017). The results of fine models generate a tensor of inherent strain values (averaged over the RV volume), and these values are used in the coarse model (macroscale) during activation of each element or each layer. This analysis of deposition process can be applied to selective laser melting (SLM) (Alvarez et al., 2016) or other similar additive manufacturing (AM) technologies (Denlinger et al., 2014). In general two approaches are typical:

- very fast "one shot" approach, where structure is analyzed in pseudo-static, linear analysis, applying thermal field determined from thermal analysis

- transient process where combined thermo–mechanical solution is computed while adding new material layer-by-layer

Some authors (Keller and Ploshikhin, 2014) apply different tensors throughout the structure, by rotating the RV tensor to align with directions of the movement of heat source; however, usually the inherent strain remains constant at all locations in the part.

Often the solution process [as advertised by various commercial solvers (ANSYS, 2017; AUTODESK, 2017)] includes some calibration, (i.e., instead of solving one RV to obtain values for inherent stress, the meso–scale model contains one or more tunable parameters). The exact nature of these parameters is usually proprietary and not published. User, are required to perform a simple experiment: build a standardized part, measure its free shape deformation, which is used internally to tune the value of the parameter(s). Such tuning is then deemed appropriate for a specific 3D-printer, material properties, and process parameters.

For the part designer, the main goal of the AM process analysis is to predict and prevent most common types of failure, where the critical ones are:

- part will have shape and dimensions different from expected because of thermal distortion during printing and residual stress left in the structure;

- part may have too much residual stress after the printing, which will weaken the structure;

- part may crack during printing or removal from the base plate;

- part may distort vertically during the printing; any upward deflection of the part, which is close to or exceeds the thickness of the single layer, will interrupt the process by the collision with the blade that levels the powder after adding new layers.

There are several additional features of the process, usually of interest to the engineer, which are beyond the scope of this article, for example:

- the microstructure of the material after repeat melting and solidification of powder grains (Wagner et al., 2017);

- surface quality, especially in the concave areas, which may significantly affect the fatigue behavior of the structure;

- sagging of the structure when overhang surface is at low angle (near horizontal) and not sufficiently supported (including buckling of support elements).

The last item usually is resolved during the design phase by avoiding low angle overhang or by creating additional structural supports. We do not include this effect, and therefore gravity forces will not be applied to the numerical model of the structure.

In addition to a typical multiscale modeling, dynamic mesh adaptivity can be used dramatically to reduce the cost of computation (Lundbäck et al., 2017), however, it is not sufficient to eliminate the need for inherent strain approach.

To assess the possibility of the above types of failure, it is important not only to compute the final shape of the structure, but also to accurately estimate displacements and stresses during the printing process (i.e., for partially built parts). Thus, at least for the latter two of above listed failure modes, it is important to solve transient thermal problems during the printing, coupled with pseudostatic solution of the partially built part at consecutive time values

during AM printing. We argue that even for approximate solution to the first two issues, it is still beneficial to solve the transient thermal processes.

In this article, we propose to use multiple mesoscale models to generate multiparameter family of approximations, and thus allow better adaptation of the values of inherent strain at each element in the macroscale model.

2. PROCESS–DEPENDENT INHERENT STRAIN APPROACH

2.1 Traditional Inherent Strain

Inherent strain is the total strain observed by an infinitesimally small volume of the material when it is removed from inside of the body (and freed from any boundary loads/constraints). The presence of inherent strain can be experimentally verified and measured in welded or AM produced parts, even if the structure has no external load, and it is usually assumed that it comes entirely from plastic deformation during the manufacturing process.

At each point in the structure, total strain ε can be decomposed into following components

$$\varepsilon = \varepsilon^e + \varepsilon^p + \varepsilon^{th} + \varepsilon^{pc} \tag{1}$$

Those are respectively: elastic strain, plastic strain, thermal strain, and strain due to phase change.

Only elastic strain contributes to the equilibrium equation, using linear elastic constitutive relation:

$$\sigma = E \cdot \varepsilon^e \tag{2}$$

Thermal strain $\varepsilon^{th} = [\alpha * (T - T_{ref})]$ is a function of current temperature T and reference temperature T_{ref} and vanishes after material is cooled down to room temperature (or whatever is considered reference temperature).

Phase change strain ε^{pc} is relatively small (Liang et al., 2017; Michaleris, 2014) and we will neglect it here.

Application of this model can be practically solved only on small specimens, and then the average strain in such a specimen after cooling down is interpreted as inherent strain in a macroscale model. Usually only diagonal terms of such strain tensors are present, and typical values differ by one order of magnitude, with max value in the vertical direction, and minimal in the direction aligned with a prevailing direction of torch movement (i.e., along the hatches). Inherent strain may be also estimated using experimental methods or calibrated using printing of standardized models and measuring characteristic deformation of produced part.

For example, Keller and Ploshikhin (2014) quotes used inherent strain tensor as:

$$\varepsilon^{inh} = \begin{pmatrix} -0.001 & 0.0 & 0.0 \\ & -0.003 & 0.0 \\ & & -0.01 \end{pmatrix}$$

Negative values on the diagonal mean that the RV represents anisotropic shrinking of the material after cooling down.

This inherent strain is then used in the analysis of the full part by assuming that the strain in any finite element is computed as

$$\varepsilon = \varepsilon^e + \varepsilon^{inh} \tag{3}$$

As the inherent strain includes effects of thermal deformation and plastic strain in the specimen, the final model need not have a thermal model solved, and solution of the global model is reduced to a (potentially single) static linear analysis. This allows for rapid computation, even with fairly detailed finite element model.

2.2 Linear Deposition Model

In this section we present an alternative interpretation to account for the inherent strain, which opens a possibility for quantitative solution of its values, without resorting to experimental measurements.

In the previous work (Bass and Liszka, 1999; Kennon et al., 1995; PhlexSolids, 2001) the traditional Finite Element formulation was extended to handle discontinuous deformation field necessary for the material deposition

process typical for semiconductor manufacturing. While that work was performed in the context of hp-adaptive finite element formulation, it can be applied to extend any standard finite element code. The main requirement is that the implementation allows option of activating/deactivating elements (sometimes called birth/death of elements).

Deposition is modeled as a linear elasticity process consisting of multiple steps, each adding or removing layer of elements (Fig. 1). Adding is performed after heating or cooling are existing partially built structure and a new layer is added in a stress-free state. However, activated elements inherit nonzero displacement from the existing neighbor elements. This displacement field is stored for each element as a reference configuration. An alternative interpretation is that the initial state of element strain is stored. In both cases, it is assumed that the reference temperature is the temperature of activating the element. In welding analysis, or AM process simulation, this is usually at or close to the melting temperature of the material.

Thus Eq. (1) becomes:

$$\varepsilon = \varepsilon^e + \varepsilon^{th} - \varepsilon^{ref} \tag{4}$$

where ε^{ref} represents initial strain at the element activation.

This results in element without any stress at the moment of its activation, despite the fact that surrounding elements (active at the preceding time step) are in the deformed state.

This process, when applied during transient thermo–mechanical process, accounts for two major sources of inherent strain:

- shrinkage of the material during cooling from melting to the room temperature, and

- deformed state of neighboring elements, caused by their thermal and mechanical state. In particular this will account for the change of the volume of each element (as neighboring elements either squeeze, or expand the space allowed for the addition of melted metal), and for the change of the shape because the part shifted from its reference configuration.

By applying/extending this deposition modeling technique to the welding, it is possible to estimate residual stresses caused by the weld connecting two distorted parts, even if that distortion is transient, result of transient thermal field. During analysis of the AM process the same mechanism is responsible for residual stresses, and for potentially misaligned parts. Figure 2 shows the case when new layer elements are activated at expected (ideal) position, however, the structure underneath is deformed, therefore new elements end up misaligned after cooling down. This mechanism of shape deformation is different than the springback, which can be simulated with much simpler inherent strain method. Moreover, this misalignment can be correctly emulated on each level (meso and macro) independently. On the meso level, it will contribute to off diagonal terms in the inherent strain for RV, and macroscale will amplify this effect for the global structure.

The above presented deposition method is applicable both on macro– and mesoscale models. On macroscale the material behaves linearly immediately after element activation: each element represents multiple layers of droplets, and nonlinear behavior is fully simulated by the inherent strain tensor evaluated from mesoscale analysis.

On mesoscale level assumption of linear material properties is not expected to be sufficient: all practical materials exhibit presence of a liquidus range, where material flow occurs, and also (unlike during the welding) material is
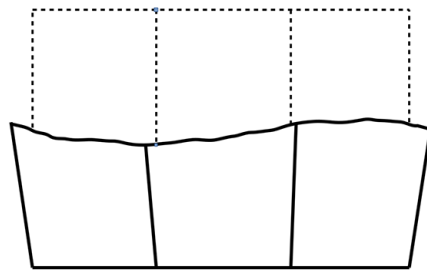
FIG. 1: Two–layer deposition. Scale of displacements is exaggerated.
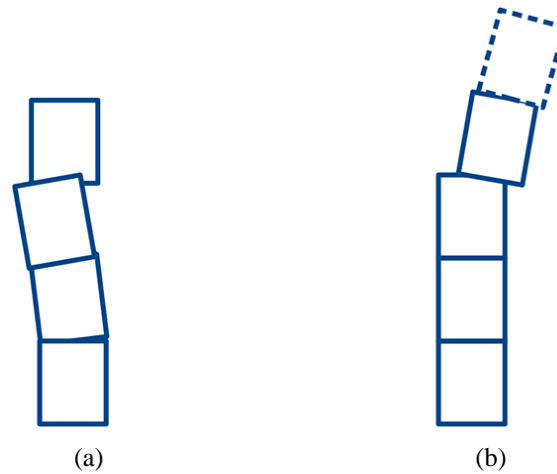
FIG. 2: Example of straight beam misalignment during AM printing. (a) Partially printed beam is bent sideways (presumably because of the thermal deformation) and new element is added on top of deformed shape, (b) final shape after cooling down, next layer (dotted line) may be even more distorted.

melted multiple times, to assure continuity of the structure. Most of weld analysis software utilizes detailed analysis of plastic deformation, especially immediately after solidification, when temperature of the material is still high. Numerical examples presented below are however limited to linear elasticity models only. In this study, our goal is to answer how meaningful is the effect of material deposition over the global structure. A linear elastic mechanical model is then the simplest model we can use to achieve this. We expect more detailed analysis later to answer how much results change due to the plastic flow.

2.3 Thermal Field Model

Accurate representation of thermal field (and resulting mechanical deformation) is essential in this process. Thermal energy balance can be represented as Zeng et al. (2012)

$$\rho \, C_p \, dT(X,t)/dt = -\nabla \cdot q(X,t) + Q(X,t), \qquad X \in \Omega \tag{5}$$

where ρ is the material density; C_p is the specific heat capacity; T is the temperature field; $q()$ is the thermal flux vector and $Q()$ is the internal heat source resulting from phase changes. Material properties ρ, C_p, and thermal expansion coefficient α are usually temperature dependent.

An important aspect of the thermal analysis is evaluation of the amount of energy generated in the structure by the torch/laser, and boundary conditions representing energy loss to the surrounding area by radiation and convection. While thermal conductivity of the powder may be often simplified by a boundary condition or even completely neglected, the heat transfer to the base is usually significant and needs to be modeled using additional layers of thermal elements or at least proper boundary conditions.

Estimating the amount of thermal energy entering the structure from a heat source is a complex problem, even for much simpler weld simulation. Different, very detailed, experimental models describing melt pool shape and size can be encountered in the literature, [e.g., Double Ellipsoid configuration or Gaussian Flux Distribution model proposed in Goldak et al. (1984); Paley and Hibbert (1975); Pavelic et al. (1969)]. Notice that energy needed to change phase (melt/solidify) has to be accounted for, however, the actual process of phase change need not be explicitly simulated for this analysis.

Once the thermal analysis is computed, the elements are activated when temperature at each element falls below the fixed value, usually equal, or slightly lower than the actual melting point for the material, or some specific temperature within the solidus range for metal alloys.

2.4 Pre-Strain

Conceptually the formulation allows each layer of elements to have independent reference displacement field, and reference temperature. As the consequence, (assuming small displacements and rotations) we have a linear solution model, which represent internal strain (inherent strain) without the need for elasto–plastic formulation.

This formulation is applied in AM process simulation in two-scale model:

- on mesoscale: to compute representative volume (RV), a cube with size of 10–20 elements across, where each finite element may be activated independently;

- on macrolevel simulation: representing full model being printed, where each finite element is much bigger than the laser tip diameter (i.e., bigger than melting pool size), and because of that the elements are activated layer-by-layer.

On the macroscale level, we assume that each element is added to the structure at the same time (when each layer is activated), it has purely linear constitutive equations, and starts with values of inherent strain computed from the mesoscale RV model. Actual values of inherent strain are not constant; they are transferred from an appropriate mesoscale model and aligned with boundary direction or laser scan direction where appropriate. For this, we expand Eq. (4) into:

$$\varepsilon = \varepsilon^e + \varepsilon^{th} - \varepsilon^{ref} + \varepsilon^{inh} \tag{6}$$

Here, ε^{inh} represents inherent strain tensor, calculated from mesoscale computation.

Again the thermal boundary conditions must be properly evaluated, in order to solve for the global temperature field in the whole structure, and resulting displacement field is discontinuous similarly to the above deposition process.

Notice that at this stage, we have a choice of performing purely mechanical analysis or thermo–mechanical analysis; the computer cost is much higher in the latter case, however, different values for ε^{inh} have to be used in these two cases. In the former case, the inherent strain represents approximation of thermal strain, and so it needs to be extracted from RV cooled to a room temperature, while in the latter case we have to avoid adding thermal dilatation again, and so the inherent strain has to be extracted from the RV cooled (heated) to the activation temperature.

2.5 Mesoscale Model Parameterization

To improve accuracy of the overall solution, we expect that the tensor representing inherent strain in each element of the global model will vary, representing different state of the structure in the vicinity of such elements. Assuming that RV is represented as a cube, following items could be considered during mesoscale analysis:

- each of 5 faces of the cube (top is always open) can be connected to a neighboring cube representing metal or powder, which requires different thermal and structural boundary conditions;

- direction of hatches relative to boundaries, and sequence of hatches in different layers (aligned or cross–hatching);

- time to cool the RV between hatches, this quantity can be estimated at the global level, and can change at each time step, as it depends on the total volume of the current layer;

- thermal gradient at the bottom of the cube may have a different value, depending on the cooling effect of neighboring layers, including effect of the base plate at the start of the process.

Additional parameters may be considered, depending on the amount of access to the printer algorithms, although in many cases those remain proprietary and cannot be evaluated or controlled externally for most commercial AM printers.

Varying the above parameters allows generation of more accurate representation of inherent strain values to be used in the global model. In addition to use of different values, the inherent stress tensor can be rotated to align with boundary and/or prevailing printing directions.

Hill-Mandel condition to determine the optimal size of RV was not applied here as the effects analyzed in this project cannot in general be represented as periodic structure (e.g., when estimating inherent strain near the free surface of the part). Thus, in all examples presented below, the size of RV was selected to match the size of elements on the macroscale level. Eventually, the process should contain more accurate estimation of 'base' value of the inherent strain including nonelastic effects and proper estimation of RV size, and the effects studied here need to be added as incremental values.

3. NUMERICAL EXAMPLES

The above thermo–mechanical solution is implemented using public domain finite element software Kratos CIMNE and TUM (2018); Lu et al. (2018).

In this section, we present a set of selected numerical results obtained by running coupled thermal mechanical analysis from a RV model with various combinations of the modeling parameters. The purpose of having the results on the same RV model is to demonstrate and study the effects of the parameters on the inherent strain tensor.

3.1 Thermo–Mechanical Properties

In preparation for the validation phase with experimental results, we used material properties provided by the industrial partner cooperating with us on this project. Thermo-mechanical properties of titanium alloy Tia6v IPC (2018) and machine parameters from an EOS M290 printing machine were used. Yield stress and young modulus vary between respectively 955 MPa and 125 GPa at 300 K and 330 MPa and 9 GPa at 1373 K, solidus temperature is 1878 K, laser velocity is 1.2 mm/ms, laser diameter 0.08 mm and hatch spacing is 0.08 mm. Laser power is 280 W and powder thickness 30 μm.

Several scanning strategies were applied, bidirectional and unidirectional along X, then crossed along X and Y (Fig. 3). In addition to the direct effect of the scanning strategy on the strain tensor, for each scanning strategy several parameters were studied in a range of values. These are: the laser velocity, the powder thickness, the number of cubes built in the same time step, and the delay at the end of each path.

3.2 Mesoscale Model: Representative Volume Setup

A cube of unit length in x, y, and z direction is used as representative volume. A Cartesian mesh is generated with 10 elements in each direction, therefore, 1000 elements in total for the cube model. In practice, the size of this cube is defined by the thickness of the deposited layer in the numerical model.

Varying parameters introduced in the model include: hatch patterns, speed of the laser, and cooling time between each layer of deposition. Based on different combinations of the parameters, different patterns of residual strain are observed. Note that the resulting strain tensor contains both diagonal and off-diagonal terms, which models the expansion or shrinkage of the material as well as the asymmetrical deformation due to specific laser scanning sequences.

Inherent strain values are extracted as an average within the center part of the cube, disregarding two external layers of elements (i.e., typically $6 \times 6 \times 6$ cube out of the $10 \times 10 \times 10$ RV) (Fig. 4).
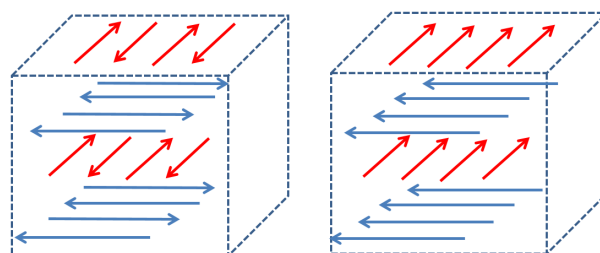

FIG. 3: Bi-directional and uni-directional scanning strategies
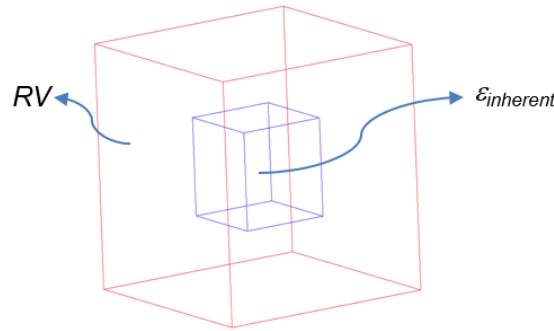
FIG. 4: Unit cell definition within RV

3.2.1 Effects of Boundary Conditions

The set of results shown in Fig. 5 demonstrate the effects of changing boundary conditions on the final distortion of the RV model. The elements in each layer are activated in groups (so-called hatch-by-hatch activation). Laser speed is set as 0.1 unit length per second, and it is the same for all three cases. Similar studies were carried out with different hatch patterns and laser speed settings, but all results are not included in this section.

Results in this and following two sections simulate RV located directly on the base plate (implemented as rigid structural support and high thermal conductivity boundary condition).

Observation: distorted configuration changes apparently due to different boundary constraints. More constraints lead to smaller final displacements.

3.2.2 Effects of Laser Speed

Figure 6 demonstrates the effect of varying laser speeds on the final distortion of the cube models.

Observation: the faster the laser speed, the less skewed the distortion becomes, resulting in lower values of off–diagonal coefficients in the inherent strain tensor.
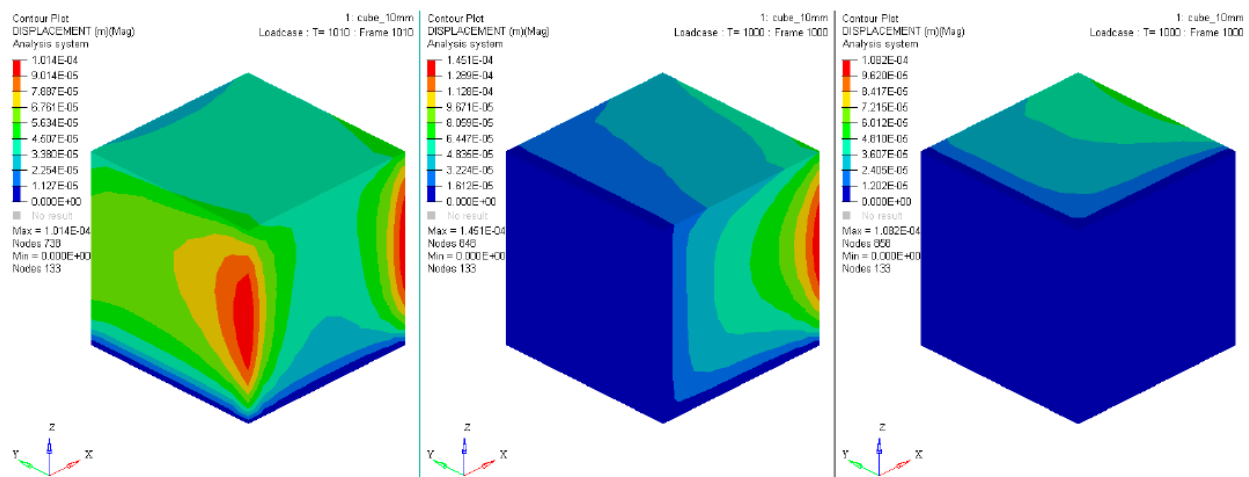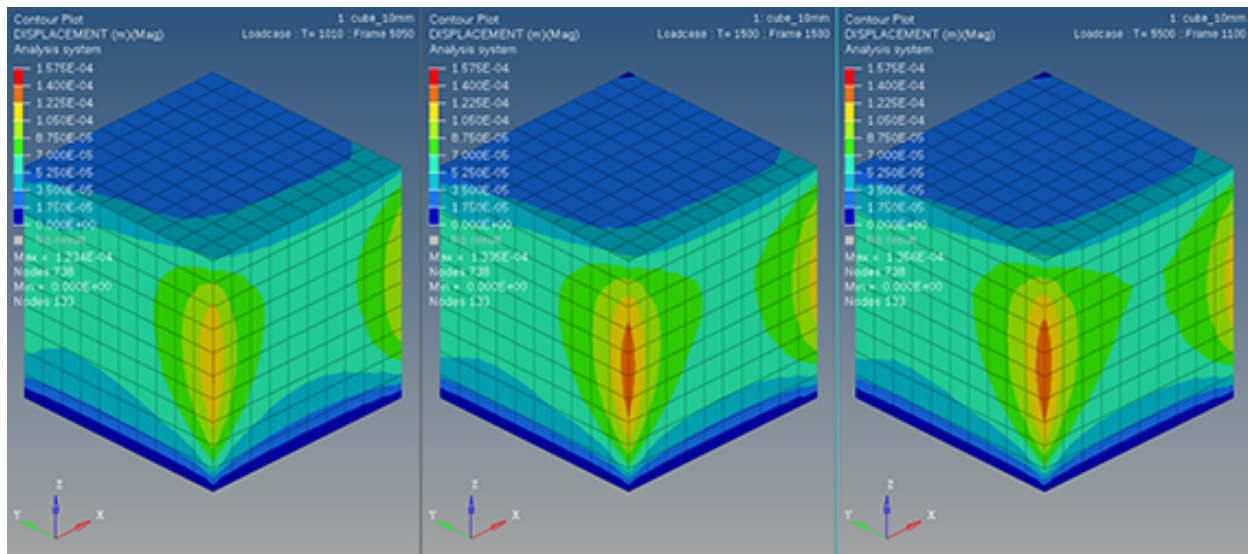

FIG. 5: Displacement results from hatch-by-hatch deposition with varying constraints to the sides of the cube geometry. (a) Bottom-sided (x-y plane) constrained, (b) with bottom (x-y plane) and left (y-z plane) sides constrained, (c) with bottom (x-y plane), left (y-z plane) and front (x-z plane) sides constrained.

FIG. 6: Displacement results from hatch-by-hatch deposition with varying time step sizes to model different scanning speeds. (a) 0.2 sec, (b) 1.0 sec, (c) 5.0 sec.

Possible explanation: as speed becomes faster and faster, deposited materials get less time to cool down, and the process becomes closer to the layer by layer process, in which case the deformation is expected to be more symmetrical. It is as if the materials are deposited more or less at the same time and get cooled down together. In the 5 sec case, it becomes closer to the approach with inherent strain. Individual groups of elements get cooled down one after another, therefore the final results show the skewness corresponding to the scanning direction.

In addition to the effect laser speed has on the solution asymmetry, one can also observe that the faster the laser speed, the less the overall displacement.

3.2.3 Effects of Hatch Pattern

Figure 7 demonstrates the effect of different hatch patterns, namely, layer-by-layer, hatch-by-hatch and element-by-element. Laser speed is set to 1.0 sec per 1/10th of the unit length.

Observation: different hatch patterns have a significant effect on the symmetry of the displacement configuration.

Also note that the study of hatch pattern is largely for use in macroscale models. For mesoscale models, we use element-by-element activation by default for better accuracy.

Figure 8 shows the effect of the scanning direction, bidirectionnal along X, crossed bidirectional alternating X and Y direction for each new printed layer, in comparison with a layer-per-layer approach. This demonstrates that in addition to the hatch pattern the scanning direction itself has a non-negligible effect on the displacements.

We can notice in Fig. 9 that stresses close to the plasticity limit appear only near to the base plate and mainly in the four corners, those layers are excluded before computing component values for the inherent strain tensor.

3.2.4 Effects of Timing and Delays in the Process

In the following group of tests we study the effect of delay between the laser returns to the same location on the nearest hatch. Here the base plate is explicitly modeled with FE, but not shown in the figures. The delay is caused by two separate effects: For a bidirectional scanning strategy, the laser is turned off to avoid overheating when the laser turns back and moves in the other direction. Much larger values of the delay must be considered when laser beam leaves the RV to cover the rest of the path outside of the RV and before crossing again the same cube on its way. In other terms, this latency is introduced to allow emulating printing layers of a different size, and the delay is directly
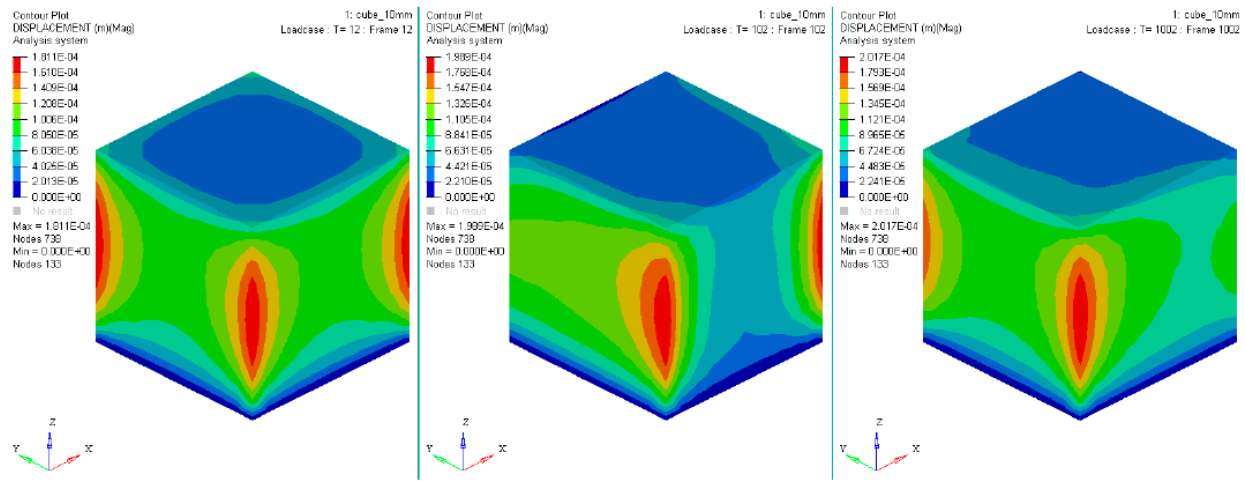
FIG. 7: Displacement results from hatch deposition with varying patterns: (a) layer-by-layer, (b) hatch-by-hatch, (c) element-by-element
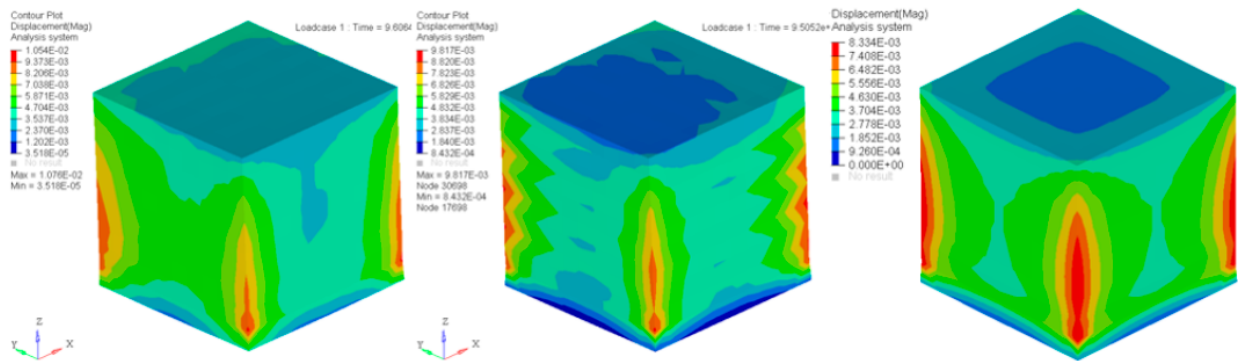
FIG. 8: Effect of scanning strategy: (a) bi-directional X, (b) crossed bi-directional XY, and (c) layer-per-layer

proportional to the total crossection of the part. In Fig. 10 we can observe that stresses and displacements are higher for a smaller latency values.

Figure 11 shows the effect of changing laser speed in a range of 0.8 up to 1.4 mm/ms for a bidirectional scanning strategy. Higher speed lowers the energy input and results in lower temperatures and smaller volumetric change of RV.

3.3 Macroscale Model

Several physical models have been analyzed using residual strain results obtained from the above analysis. At this stage of the project, all results are presented using fixed inherent strain tensor (i.e., potential variability of inherent strain is not tested here).

In all presented examples the macroscale model is built on pure mechanical analysis with linear elastic material properties (no thermal analysis is performed on a macro model and thus the computed distortion results directly from the imposed inherent strain values).
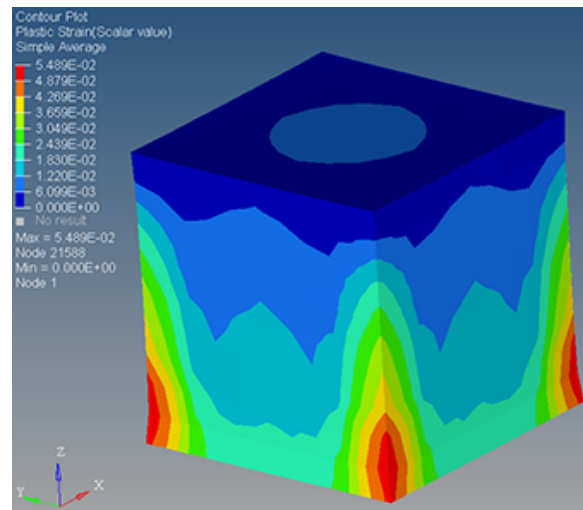
FIG. 9: Stress results for the layer-per-layer scanning strategy. Red color shows zones locally exceeding yield stress level.
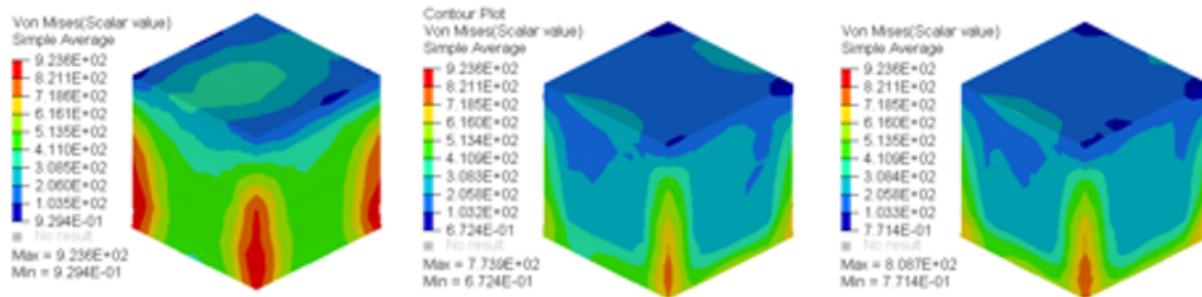

FIG. 10: Von Mises stress level respectively: no latency delay, 0.2 ms and 0.5 ms
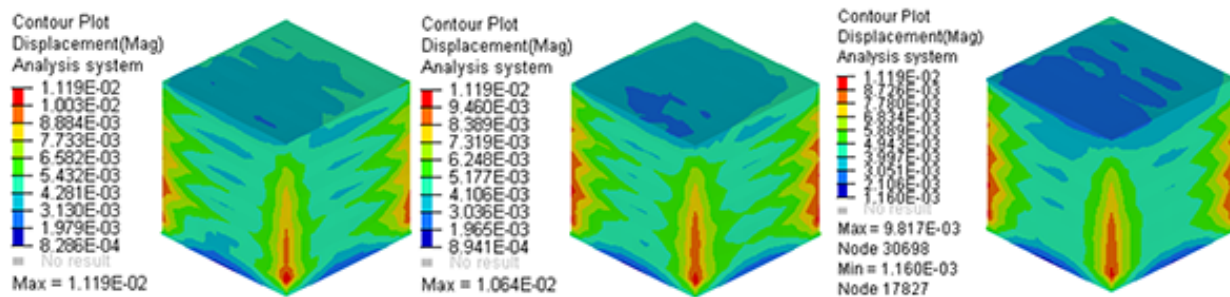

FIG. 11: Displacement for different scanning speed, respectively 0.8, 1.2, 1.4 mm/ms

3.3.1 Bracket

This model represents a shape resulting from topology optimization. The CAD model contains the workpiece to be printed, the support structures designed to minimize distortion and the base plate of the printer. Layered tet elements are used. The total height of the bracket is 44 mm. Total number layers used for activation is 44 with layer thickness being 1 mm. The mesh has about 430 thousand nodes and 2.0 million tet elements. The model was solved on a Desktop workstation equipped with Intel Xeon E5-2640 v4 CPUs at 2.40 GHz. Solving with 20 cores, the total wall time was 3793.5 seconds (about 1 hour).

Figure 12 shows displacements with symmetrical orthotropic inherent strain tensor. Figure 13 shows displacements with asymmetrical generic inherent strain tensor.

3.3.2 Filter with Lattice Structure

In this section, a model with a lattice type of middle section is presented. It is intended to represent typical metal filters. A voxel mesh is generated for this model with about 247 thousand nodes and 186 thousand elements. The height of the model is 220 mm and layer thickness of 1 mm was chosen for the simulation. The model was solved on the same workstation used for the Bracket model. The total wall time was 8285.2 seconds (about 2.3 hours).

Figure 14 shows two sets of displacement results with different element activation methods. In one case, elements are activated layer after layer with inherent strain being accounted for at the moment of activation. As a result, displacements are accumulated layer-per-layer. In the other case, all the elements are activated at the same time. As a result, one can observe the global effect of shrinkage due to cooling, but the accumulation of internal strain due to the build process is lost.

3.3.3 Valve

This model is a part from an industrial application and has been designed by Alstom for the Maestro European project (CORDIS, 2016). The bottom part of the valve body started as solid part. The middle section and top part are then 3D-printed to arrive at the final shape of the valve. Layered tet elements have been used to discretize the model and
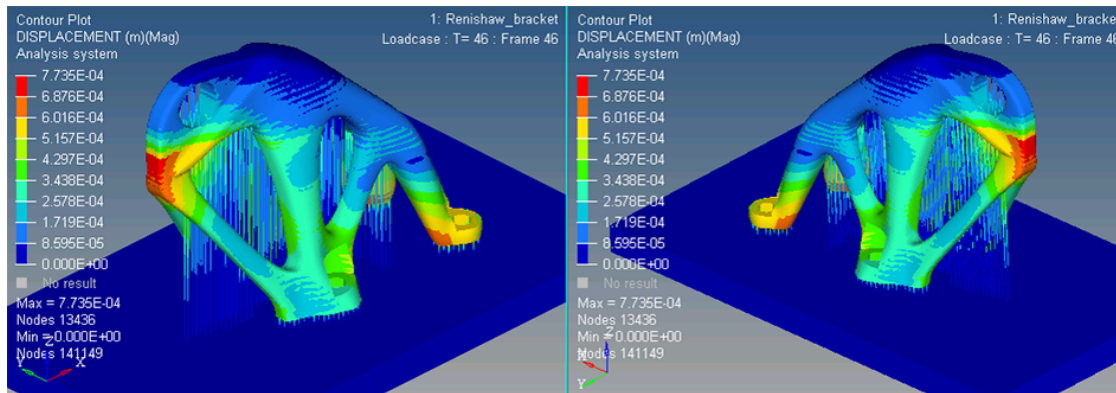

FIG. 12: Displacements with orthotropic inherent strain tensor (with zero off-diagonal values)
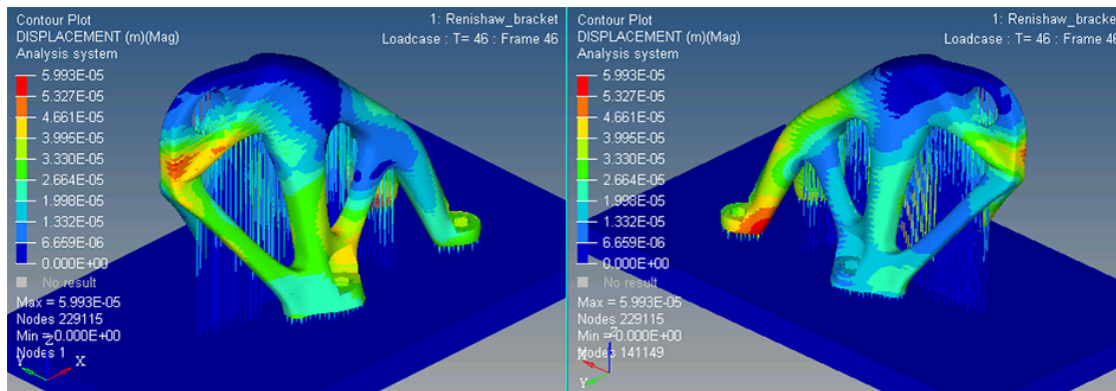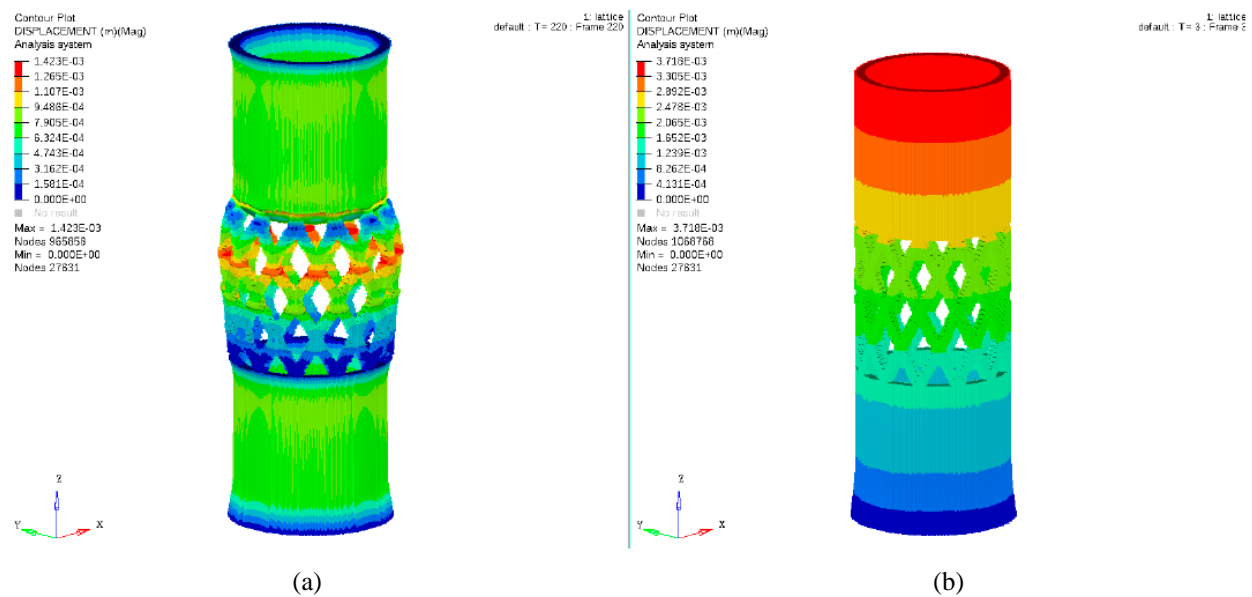

FIG. 13: Displacements with full inherent strain tensor with nonzero off-diagonal values

FIG. 14: Displacement results with (a) layer-by-layer deposition process, and (b) single-step deposition process

the mesh has 112 K nodes and 481 K elements. Solved with the same computer as the previous models. The height of the model is 94 mm and total number of layer being used is 94. The total wall time was 2158.6 seconds (about 40 minutes).

Three snapshots of the simulation results are shown in Fig. 15. The purpose is to demonstrate the merit of using time dependent transient inherent strain process versus the convectional one-shot inherent strain simulation. One of many benefits of the transient simulation is the ability to detect possible blade crash as it happens. It was reported that attempts to print similar part resulted in a edge collision near the bottom of the structure, coinciding with the location where our numerical results show large upward displacements.

3.3.4 Antenna

This is another model from an industrial application. In this case, we show the difference between using coarse (or large) layers of elements versus using fine (or small) layers. The mesh for this model consists of layered tet elements with 77 K nodes and 351 K elements, solved with the same computer as the previous models. The height of the model was 136 mm. In the case of using coarse layers, the thickness of an individual layer was set to be 10 mm and total number of layer being used was 14. The total wall time was 205.2 seconds. In the other case where fine layers were used, the thickness of each layer was set to be 1 mm and total number of layers was 136. The total wall time for the fine layer case was 1812.6 seconds. It is quite obvious that the increased simulation time is due to the fact that more layers require simply more solution steps. Figure 16 shows the final displacement results for the coarse layered model versus the fine layered model. Figure 17 compares numerical results with available experimental data.

4. CONCLUSIONS AND FUTURE STUDIES

This article presents an initial study of possible enhancements of a well-known inherent strain method to obtain better prediction of stress and distortion during the process of SLM. Presented numerical examples show that including better estimates of inherent strain (including in particular off–diagonal terms in the strain tensor) and varying this strain during the process can substantially change results and hopefully provide better correlation with the values measured during experiments.

(a)

(b)

(c)

(d)
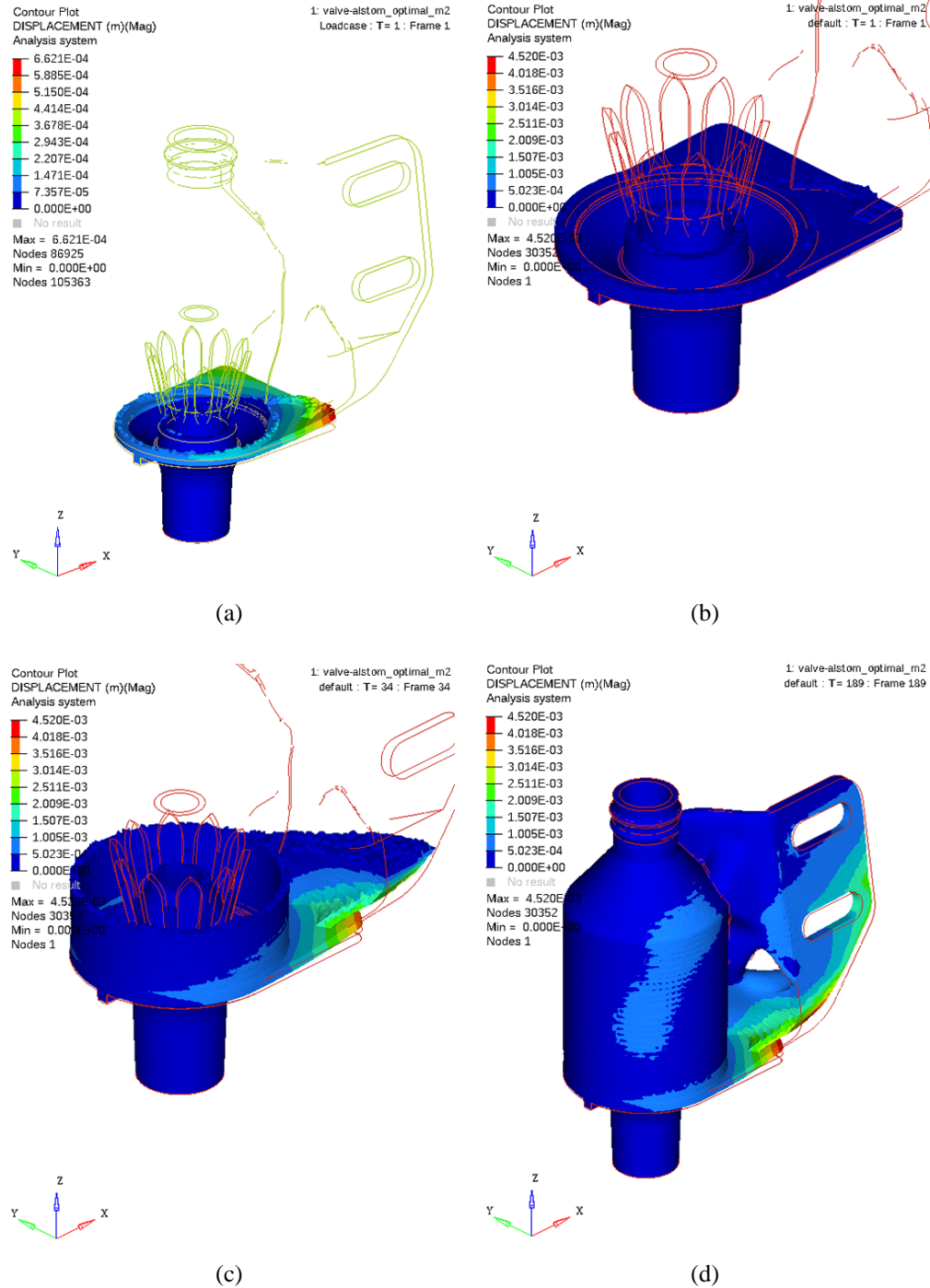
FIG. 15: Displacement results of the valve model [courtesy of Alstom for the European Maestro project CORDIS (2016)]. (a) The top-left figure shows a snapshot of the entire part at the early stage of the printing process. (b) The top-right figure shows the starting point of the bottom part of the valve which is equivalent to a base plate. (c) The bottom-left figure shows a snapshot of the distortion of the part being printed, and (d) the bottom-right figure shows the final distortion of the entire part at the end of the deposition process.
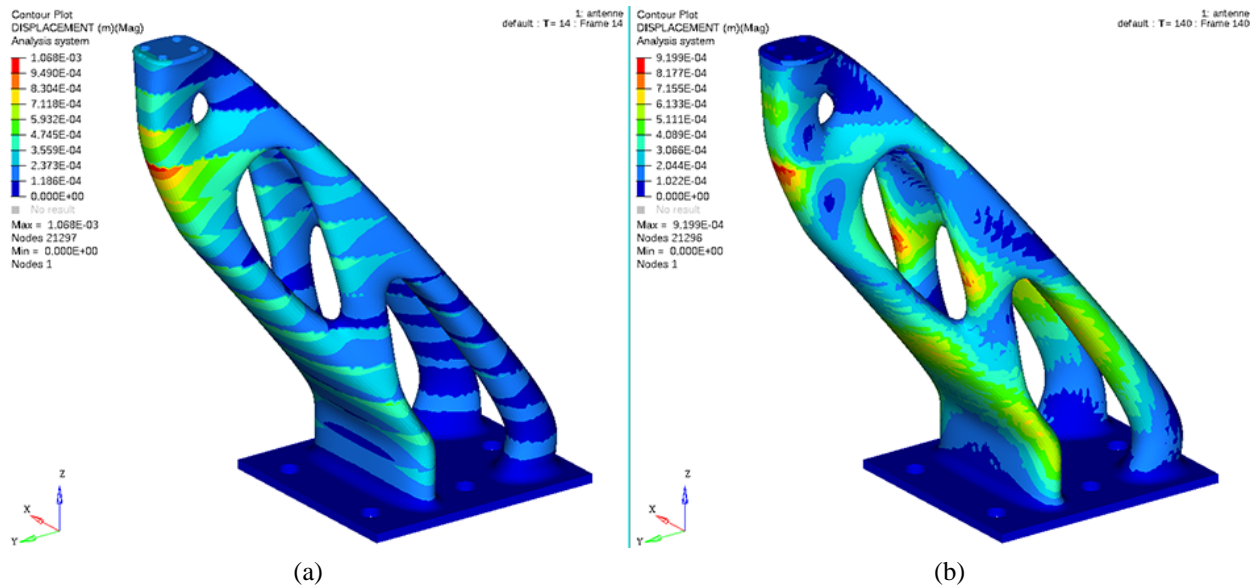
FIG. 16: Displacements (a) with coarse 8 mm-layers and (b) fine 1 mm-layers
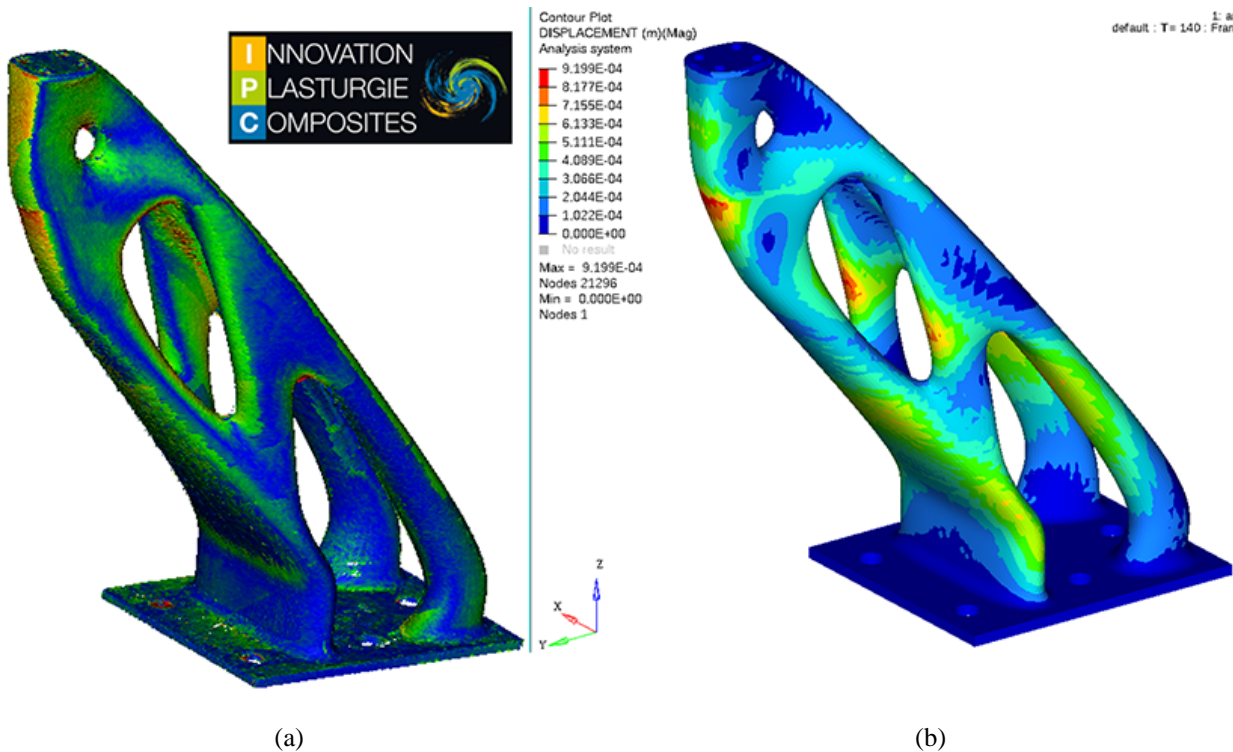

FIG. 17: (a) printed part 3D scan of difference with the CAD geometry (reprinted with permission from the IPC Company), (b) numerical results for the same geometry

However, at this stage of the work, only the outline of this process has been implemented in the computer code, and the results show that these enhancements can influence the outcome. The effects of the boundary conditions

timing parameters, and of the printing pattern have been presented and tested. Varying inherent strain values within the structure, and the effects of other factors (e.g., temperature gradients) remain as the future expansion.

Once the results of numerical process are available for a practical example, the next phase of the project will involve experimental verification of these results, in cooperation with supporting companies listed below. Only after experimental confirmation, we would be able to decide which of the described corrections can and should be included in the proposed commercial software.

ACKNOWLEDGMENTS

REFERENCES

Alvarez, P., Ecenarro, J., Setien, I., San Sebastian, M., Echeverria, A., and Eciolaza, L., Computationally Efficient Distortion Prediction in Powder Bed Fusion Additive Manufacturing, *Int. J. Eng. Res. Sci.*, vol. **2**, pp. 39–46, 2016.

ANSYS, Additive Manufacturing Simulation, accessed Sept. 20, 2018, from https://www.ansys.com/products/structures/additive-manufacturing, 2017.

Argyris, J.H., Szimmat, J., and Willam, K.J., Computational Aspects of Welding Stress Analysis, *Comput. Methods Appl. Mech. Eng.*, vol. **33**, pp. 635–665, 1982.

AUTODESK, Autodesk–Fusion–360, accessed Sept. 20, 2018, from https://www.autodesk.com/products/fusion-360, 2017.

Bass, J. and Liszka, T., HP-Adaptive Analysis of Thermal Stresses during Deposition Process, Altair Engineering, Project Proposal for Motorola Company, 1999.

CIMNE and TUM, Kratos Multi–Physics, International Center for Numerical Methods in Engineering, Barcelona, Spain and TUM Chair of Structural Analysis Technical University of Munich, Germany, accessed Sept. 20, 2018, from http://www.cimne.com/kratos/, 2018.

CORDIS, Horizon 2020, Project 723826: Maestro, European Commission, Community Research and Development Information Service, accessed Sept. 20, 2018, from https://cordis.europa.eu/project/rcn/205398_en.html, 2016.

Denlinger, E., Irwin, J., and Michaleris, P., Thermomechanical Modeling of Additive Manufacturing Large Parts, *J. Manufacturing Sci. Eng.*, vol. **136**, p. 061007, 2014.

Ferencz, R., Hodge, N., Ganeriwala, R., and Vignes, R., Experience and Challenges with Part-Scale Modeling of Select Laser Melting Additive Manufacturing, *14th U.S. National Congress on Computational Mechanics*, 2017.

Friedman, E., Thermomechanical Analysis of the Welding Process using the Finite Element Method, *ASME J. Pressure Vessel Technol.*, vol. **97**, pp. 206–213, 1975.

Goldak, J., Chakravarti, A., and Bibby, M., A New Finite Element Model for Welding Heat Sources, *Metallurg. Trans. B*, vol. **15**, no. 2, pp. 299–305, 1984.

Hill, R., Elastic Properties of Reinforced Solids: Some Theoretical Principles, *J. Mech. Phys. Solids*, vol. **11**, pp. 357–372, 1963.

Hodge, N. and Ferencz, R., Part-Level Finite Element Simulation of Selective Laser Melting, *14th U.S. National Congress on Computational Mechanics*, 2017.

IPC, Innovation Plastirgie Composites Center, from https://ct-ipc.com, 2018.

John, T., Goals of the Exascale Additive Manufacturing Project (Exam), *14th U.S. National Congress on Computational Mechanics*, 2017.

Kale, S., Saharan, A., Koric, S., and Ostoja-Starzewski, M., Scaling and Bounds in Thermal Conductivity of Planar Gaussian Correlated Microstructures, *J. Appl. Phys.*, vol. **117**, p. 104301, 2015.

Keller, N. and Ploshikhin, V., New Method for Fast Predictions of Residual Stress and Distortion of am Parts, *Solid Freeform Fabrication Symposium*, Austin, TX, pp. 1229–1237, 2014.

Kennon, S.R., Berry, C., Liszka, T., and Gonik, S., Phlex: An H-P Adaptive Finite Element Kernel for High Performance Solution of Problems in Computational Mechanics, *3rd U.S. Natl. Congress on Comp. Mech.*, Dallas, TX, USA, 1995.

Liang, X., Chen, Q., Cheng, L., Yang, Q., and To, A., A Modified Inherent Strain Method for Fast Prediction of Residual Deformation in Additive Manufacturing of Metal Parts, *Proc. 28th Annual International Solid Freeform Fabrication Symposium*, Austin, TX, 2017.

Lu, Q., Beauchesne, E., Liszka, T., and Reddy, M., Development of Commercial Finite Element Software using Kratos Multiphysics Framework, *13th World Congress on Computational Mechanics*, New York City, USA, 2018.

Lundbäck, A., Modelling and Simulation of Welding and Metal Deposition, PhD Thesis, Luleå University of Technology, 2010.

Lundbäck, A., Malmelov, A., Lindwall, J., and Lindgren, L.-E., Simulation of Additive Manufacturing and Techniques to Reduce the Computational Time, *14th U.S. National Congress on Computational Mechanics*, 2017.

Michaleris, P., Modeling Metal Deposition in Heat Transfer Analysis of Additive Manufacturing Processes, *Finite Elements Anal. Design*, vol. **86**, pp. 51–60, 2014.

Paley, Z. and Hibbert, P.D., Computation of Temperatures in Actual Weld Designs, *Welding J. Res. Suppl.*, vol. **54**, pp. 385s–392s, 1975.

Pavelic, V., Tanbakuchi, R., Uyehara, O.A., and Myers, P.S., Experimental and Computed Temperature Histories in Gas Tungsten Arc Welding of Thin Plates, *Welding J. Res. Suppl.*, vol. **48**, pp. 295s–305s, 1969.

PhlexSolids, *PHLEXSolids User's Manual*, Troy, MI: Altair Engineering Inc., 2001.

Shapiro, A., Additive Manufacturing for Aerospace Flight Applications, *J. Aerospace Rockets*, pp. 952–959, 2016.

Ueda, Y., Murakawa, H., and Ma, N., *Welding Deformation and Residual Stress Prevention*, Elsevier, 2012.

Wagner, G., Lin, S., and Liu, W.K., Multi-Scale Solidification Simulations of Additive Manufacturing Process in Metals, *14th U.S. National Congress on Computational Mechanics*, 2017.

Yuan, M. and Ueda, Y., Prediction of Residual Stresses in Welded T-and I-Joints using Inherent Strains, *J. Eng. Mater. Technol.*, vol. **118**, pp. 229–234, 1996.

Zeng, K., Pal, D., and Stucker, B., A Review of Thermal Analysis Methods in Laser Sintering and Selective Laser Melting, *Proc. Solid Freeform Fabrication Symp.*, Austin, TX, 2012.